Curt S. Kothera
Research Engineer
Mem. ASME
Techno-Sciences, Inc.,
Beltsville, MD 20705
e-mail: kotherac@technosci.com

Mamta Jangid
Graduate Research Assistant
Department of Aerospace Engineering,
Smart Structures Laboratory,
University of Maryland,
College Park, MD 20742

Jayant Sirohi
Assistant Professor
Department of Aerospace Engineering and
Engineering Mechanics,
University of Texas at Austin,
Austin, TX 78712
e-mail: jayant.sirohi@mail.utexas.edu

Norman M. Wereley[1]
Professor
Fellow ASME
Department of Aerospace Engineering,
University of Maryland,
College Park, MD 20742
e-mail: wereley@umd.edu

Experimental Characterization and Static Modeling of McKibben Actuators

McKibben actuators are pneumatic actuators with very high force to weight ratios. Their ability to match the behavior of biological muscles better than any other actuators has motivated much research into the characterization and modeling of these actuators. The purpose of this paper is to experimentally characterize the behavior of McKibben artificial muscles with basic geometric parameters, and present a model that is able to predict the static behavior accurately in terms of blocked force and free displacement. A series of experiments aimed at understanding the static behavior of the actuators was conducted. The results for three different lengths (4 in., 6 in., and 8 in.), three diameters (1/8 in., 1/4 in., and 3/8 in.), and one wall thickness (1/16 in.) at pressures ranging from 10 psi to 60 psi illustrate the key design trends seen in McKibben actuator geometry. While existing models predict this static behavior, there are varying degrees of accuarcy, which motivates the present study. Using knowledge gained from the experimental study, improvements for the two modeling approaches were explored, including effects from elastic energy storage, noncylindrical shape, and variable thickness. To increase model accuracy, another set of experiments was used to characterize the elasticity of the rubber tubes and fibers of the braid. Comparisons of the measured data to the improved model indicate that the ability to accurately predict the static behavior of McKibben actuators has increased. [DOI: 10.1115/1.3158982]

1 Introduction

McKibben actuators are a class of compliant pneumatic actuators with very high force to weight ratios, that are composed of an elastomeric bladder inside a braided mesh sleeve. The initial conception of these actuators stemmed from work with orthotic devices for polio patients by McKibben in the 1950s [1,2]. This work subsequently led to a patent on the actuator as a fluid-driven stroking device [3]. By applying pressure inside the elastomeric bladder, these actuators can produce large forces and undergo large contractions through dimensional changes and geometric constraints. The characteristics, along with their inherent flexibility, allowed McKibben actuators to simulate the behavior of biological muscles much better than conventional actuators [4,5]. Several names in the literature are synonymous with McKibben actuators, such as air muscles, rubbertuators, and braided pneumatic actuators. However, these are not to be confused with similar contractile actuation devices that have no braided mesh sleeve [6], with pleated bladders [7], or those with pressure controlled through ion transport [8]. A comprehensive review of all types of pneumatic artificial muscles (PAMs) can be found in Ref. [9].

The encouraging response properties exhibited by McKibben muscles have provided much motivation for research. There have been characterization studies that focused exclusively on identifying static and dynamic responses [10], fatigue limits [11,12], and applicability to robotic systems. These systems are typically centered around the manipulation and joint control of robotic arms [13–17], legs [18–20], or human assistance and rehabilitative devices, for which McKibben actuators were initially envisioned [21–23]. Numerous model formulations varying in complexity have also been proposed. Design guidelines from the past experimental studies note that higher stiffness actuators (or braids) produce more work per cycle [10], braids initially aligned closer to the longitudinal axis lead to larger contraction and force [24], latex bladders offer higher fatigue life than silicone bladders [11], the use of tighter weaved braids increases fatigue life [12], and reducing the internal air volume can lead to higher bandwidth operation [25]. However, there is yet to be an investigation into the effects of various lengths and diameters, which is the first focus of this work.

Mathematical actuator models relating the force generated to the length contraction and applied pressure are typically derived from considerations for the change in volume based on the principle of virtual work [26], but other derivations consider force balancing [27], fiber-reinforced membrane analysis [28,29], and nonlinear identification [30]. However, due to the complexity involved in the system, there are still refinements that can be made to improve physical understanding. These existing model inaccuracies have led to a variety of improvement efforts, including the storage of elastic energy in the bladder material [31], noncylindrical shape at the ends of the actuator [28,32], stresses built up from an increasing diameter [25], and effects from the braided mesh [24]. The second purpose of this work is to build upon existing model formulations to further increase the accuracy and understanding of the quasistatic response of McKibben actuators in terms of blocked force and free displacement (contraction). This modeling effort will be initiated and validated with an experimental characterization of the behavior of these artificial muscles for a range of basic geometric parameters.

The remainder of this paper is divided into three sections. In Sec. 2, discussion follows a series of experiments aimed at understanding the static behavior of McKibben actuators, and the relationships that exist between different geometrical parameters. Then improvements for the two leading model derivations (energy

[1]Corresponding author.

Contributed by the Design Innovation and Devices Committee of ASME for publication in the JOURNAL OF MECHANICAL DESIGN. Manuscript received March 19, 2008; final manuscript received April 30, 2009; published online August 19, 2009. Review conducted by Diann Brei. Paper presented at the 2006 ASME International Mechanical Engineering Congress (IMECE2006), Chicago, IL, November 5–10, 2006.

Table 1 Dimensions of McKibben actuators

No.	L_0 (in.)	ID (in.)	OD (in.)	t_0 (in.)	α (deg)	n	AF_{braid}
2a	4	1/8	1/4	1/16	40.1	32	0.067
2b	6	1/8	1/4	1/16	40.1	32	0.067
2c	8	1/8	1/4	1/16	40.1	32	0.067
3a	4	1/8	1/4	1/16	61.8	48	0.101
3b	6	1/8	1/4	1/16	61.8	48	0.101
3c	8	1/8	1/4	1/16	61.8	48	0.101
4a	4	1/4	3/8	1/16	48.0	48	0.061
4b	6	1/4	3/8	1/16	48.0	48	0.061
4c	8	1/4	3/8	1/16	48.0	48	0.061
5a	4	3/8	1/2	1/16	47.1	108	0.098
5b	6	3/8	1/2	1/16	47.1	108	0.098
5c	8	3/8	1/2	1/16	47.1	108	0.098

and force balance) are explored in the Sec. 3, where some of the refinements investigated were motivated by observations and results from the experimental characterization. For example, noncylindrical tip shape was visually apparent during experimentation, and test results illustrated that bladder thickness plays a role in actuator performance and model predictive ability. The work is concluded with summary and future directions in dynamic characterization and modeling.

2 Static Response Characterization

In order to characterize the performance of the McKibben actuators, each was experimentally tested. The test specimens are composed of 18 in-house fabricated actuators with various dimensions of length and diameter. Three inner diameter tube sizes (3.175 mm, 6.35 mm, and 9.525 mm) and nominal lengths (101.6 mm, 152.4 mm, and 203.2 mm) were used, all with a thickness of 1.5875 mm. Table 1 shows a complete list of the various actuators used (in English units). Also included in the table is the number of fibers n in the different braids used to make the actuators, and the fraction of the cross-sectional area taken by the braid material, which ranges from 6% to 10%.

The test setup is shown in Fig. 1. Quasistatic testing was performed with an Instron 8841 servo-hydraulic, table top, dynamic and fatigue testing machine. This apparatus measured both load and position. Pressure was supplied to the actuator by a Jun-Air/Newport air compressor, and it was monitored with a 200 psi (gauge) (1.40 MPa) transducer from Omega Engineering, Inc., which was powered with a 24 V dc power supply. An accumulator was also added to the pneumatic circuit near the pressure transducer and actuator to help mitigate any potential fluctuations in the pressure. Data was collected on a host computer using LABVIEW version 6.1 software.

A single test run is programmed to collect both static measurements (blocked force and free contraction). At the beginning of each test, the McKibben actuator was pressurized to a specific value (10–60 psi (gauge) (415 kPa) in 10 psi (gauge) (70 kPa) increments), while holding the ends fixed. This provided a measurement of the blocked force as a function of applied pressure. It should be noted here that the pressure was maintained constant throughout each test. Then the test machine grip at one end of the actuator is unlocked and programmed to perform a slow load ramp, allowing the sample to contract until the force measurement reaches zero. This position is recorded as the free contraction measurement. Note that the quasistatic force-contraction profile at constant pressure is approximately linear. This procedure was followed twice at each test condition for each actuator, and the results to be shown represent the average.

The above set of experiments was used to characterize the behavior of McKibben actuators with respect to the following parameters: pressure, length, inner diameter, ratio of bladder thickness to inner diameter, and braid angle. As will be seen in the modeling discussion, these parameters either influence directly or indirectly the output behavior of the PAMs.

Pressure. Figs. 2–4 show the experimental results for the pressure response of the key actuator output characteristics for actuators 5c. Data from the two experiments are plotted in each of these

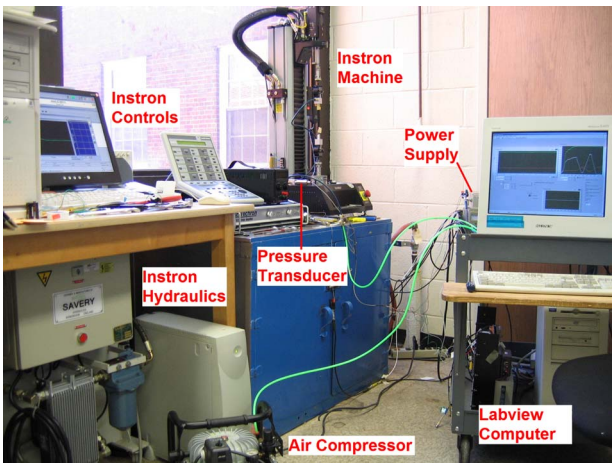

Fig. 1 Experimental setup for McKibben actuator characterization

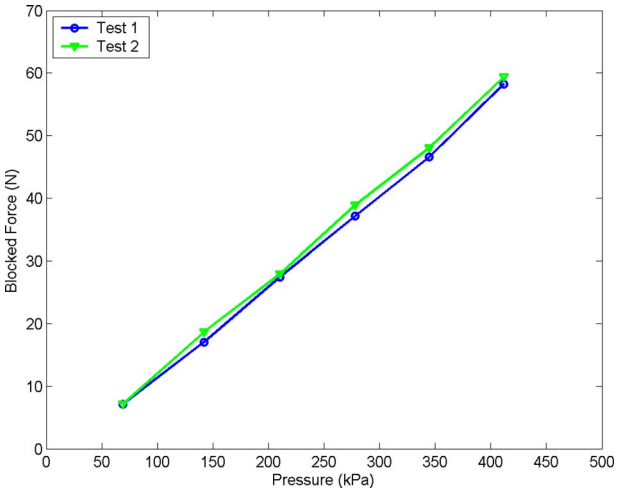

Fig. 2 Blocked force as a function of pressure—linear increase (actuator 5c)

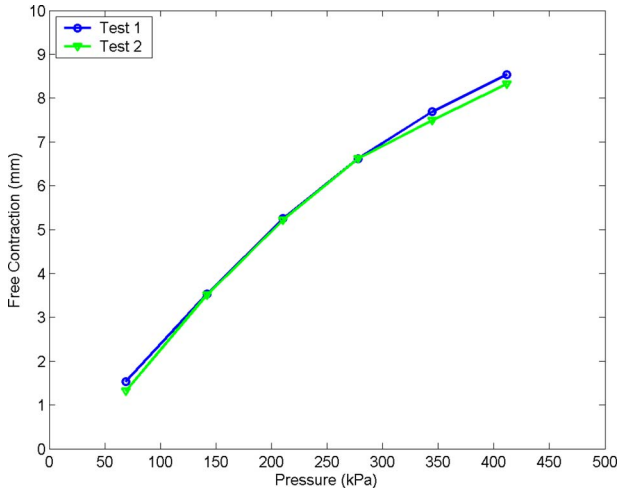

Fig. 3 Free contraction as a function of pressure—nonlinear increase (actuator 5c)

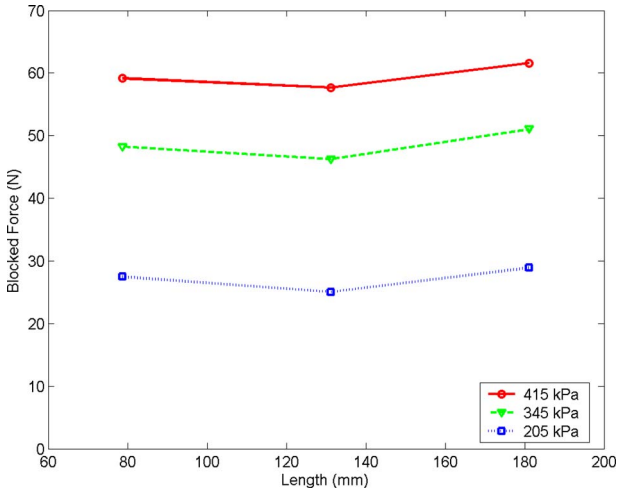

Fig. 5 Blocked force as a function of actuator length—independent (actuator 5x)

first figures to show the repeatability of the tests. The blocked force (Fig. 2) shows a linear increase with pressure, while the increase in free contraction with pressure (Fig. 3) follows a nonlinear relationship, which tends to level off with increasing pressure as the reorientation of the braid fibers begins to reach a physical constraint. Several existing models that analyze the braid angle behavior specifically make note of this effect. Free contraction gives a dimensioned maximum stroke of the actuator (e.g., ΔL_F), but it is also common to express this quantity in nondimensional form as the free contraction ratio ($\lambda_F = 1 - \Delta L_F / L_0$). These results are presented in Fig. 4. Similar to Fig. 3, there is a nonlinear relationship with increasing pressure, though this quantity decreases with increasing pressure since smaller values of the contraction ratio λ imply larger physical stroke of the actuator.

Length. Beginning with the blocked force measurements, Fig. 5 appears to indicate that this performance metric is independent of actuator length. This is true since the force is created through radial expansion (diameter increase), and increasing the resting length of an actuator will have no effect on this or the associated braid angle. The converse is true for free contraction, however. Figure 6 shows that the maximum stroke of an actuator increases with length. In each of these two figures, the increase in performance with pressure is also shown again with data displayed from three different pressure settings. Note that the length of the actuator does not affect its static behavior if we consider λ_F instead of ΔL_F. Actuators of type 5a, 5b, and 5c demonstrate this independent trend in Fig. 7, which shows little variation in λ_F as an actuator is increased in length from 100 mm to 200 mm. Since λ_F appears to be constant with L, this also supports the trend in Fig. 6 that free contraction increases linearly with length. Also note that increasing the pressure causes a decrease in λ_F as the actuator contracts more. The small variations seen here could be attributed somewhat to fabrication dissimilarities, though the model development will show that the effect of noncylindrical tips also plays a role.

Inner diameter. Actuators 3c, 4c, and 5c are compared while examining the influence of the inner diameter of the tube on the output force and stroke characteristics. Figure 8 shows the nonlinear trend of increasing force capability with increasing actuator diameter. The apparent quadratic shape of this nonlinear trend is supported in the modeling, as it will be shown that the dominant component is the Gaylord term, which states that force is proportional to the change in volume with respect to length. Assuming a perfectly cylindrical actuator with $V = \pi D^2 L / 4$ helps highlight this behavior. Figure 9 shows a nonlinear increase in stroke with diameter that tends to level off for larger sizes. The free contraction ratio λ_F behaves similarly to ΔL_F, but Fig. 10 shows that the trend

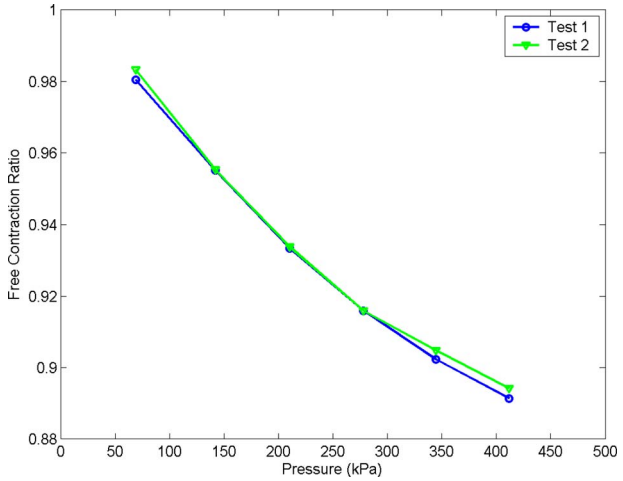

Fig. 4 Free contraction ratio as a function of pressure—nonlinear decrease (actuator 5c)

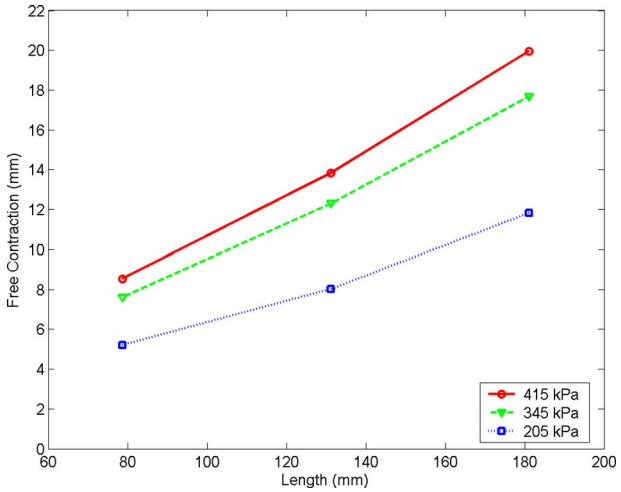

Fig. 6 Free contraction as a function of actuator length—linear increase (actuator 5x)

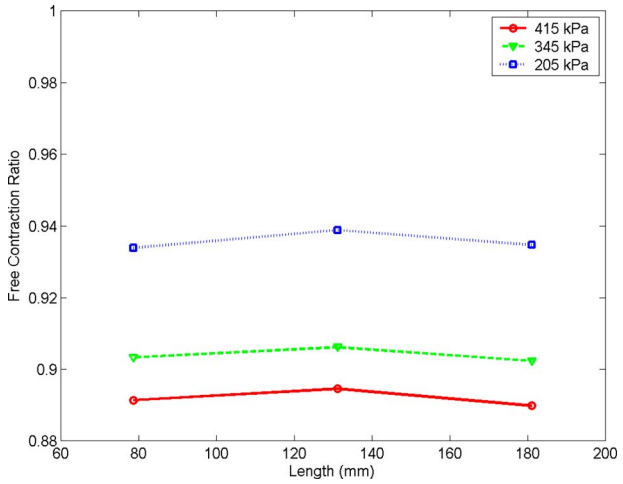

Fig. 7 Free contraction ratio as a function of actuator length—independent (actuator 5x)

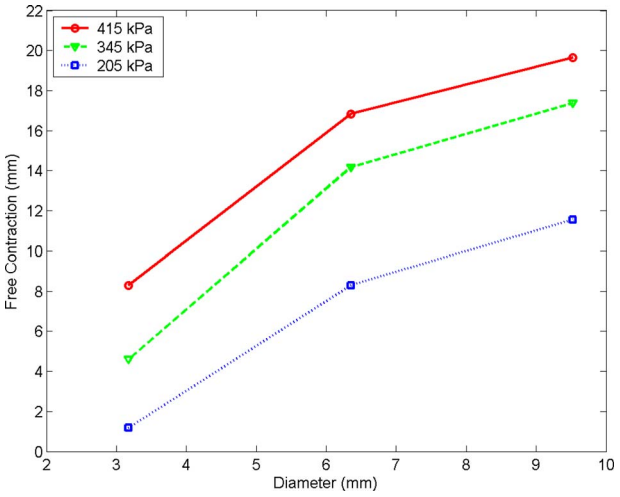

Fig. 9 Free contraction as a function of actuator diameter—increasing (actuator Xc)

is decreasing. A portion of this leveling off characteristic seen here is likely attributable to the noncylindrical tip effects, which have shown through experimental observation to be more substantial with larger diameter actuators.

Thickness to inner diameter ratio. To understand the influence of bladder thickness, the parameter t/D can be examined, as it is also a measure of how much rubber is used in the actuator by volume. Note that this ratio in the figures to be shown is taken at rest (no pressure) since t/D varies decreasingly during contraction. Actuators 3c, 4c, and 5c are again chosen to investigate the influence. A larger volume of rubber implies more energy storage and, therefore, less actuation is expected from higher t/D actuators. This is supported by the experimental results shown in Figs. 11 and 12. The blocked force F_B decreases nonlinearly with increasing t/D and tends to level off at larger thicknesses, and ΔL_F also decreases, though linearly. Likewise, the variation in λ_F is also linear, as seen in Fig. 13, though it is increasing here. Reasons for the nonlinearity here are likely attributable to the dependence of force on area, as described with inner diameter. Again, increasing pressures lead to more blocked force and free contraction, with lower free contraction ratios.

Braid angle. The braid angle is defined here as the angle between the fibers and the plane perpendicular to the actuator length (at rest), and it is used to determine the number of turns of the braid fiber around the bladder N through the relationship $\cos(\alpha) = N\pi D/B$. We can see that as the diameter of the actuator increases, the braid angle decreases for a fixed nominal braid size B. As the braid angle becomes smaller, there is less room for it to reduce further through its normal radial expansion as the fibers approach alignment with the perpendicular axis, which will lead to less actuation force and stroke. This behavior is best observed with actuators $2x$ and $3x$ $(x=a,b,c)$, which have the same diameter and thickness, but different braids. The blocked force results for actuators 2a and 3a are shown in Fig. 14. It is seen here that there is a greater sensitivity to applied pressure for larger initial braid angles, as well as higher force capability. The same trend is nearly replicated for the two stroke metrics in Figs. 15 and 16, though the contrary is shown at 205 kPa. It should be noted here that there were some inconsistencies observed in the experiments at low pressures due to fabrication inconsistencies, where the braid may not have been tightly wound around the bladder. In this case, a nominal pressure was required initially before force or motion could be generated, but this effect became negligible as applied pressure increased, which is evident in the figures. While larger initial braid angles do result in larger force and stroke capabilities, this does not come without cost. Though not portrayed in this set of characterization experiments, radial expansion (di-

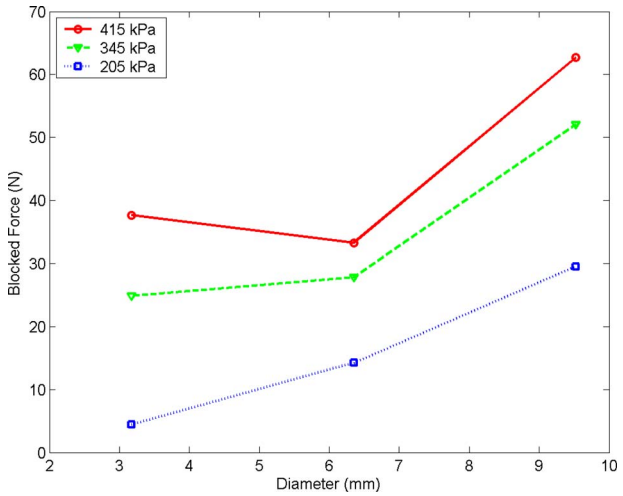

Fig. 8 Blocked force as a function of actuator diameter—quadratic increase (actuator Xc)

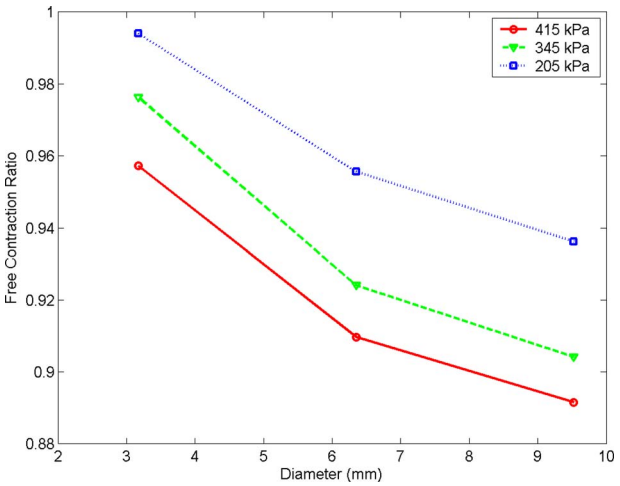

Fig. 10 Free contraction ratio as a function of actuator diameter—decreasing (actuator Xc)

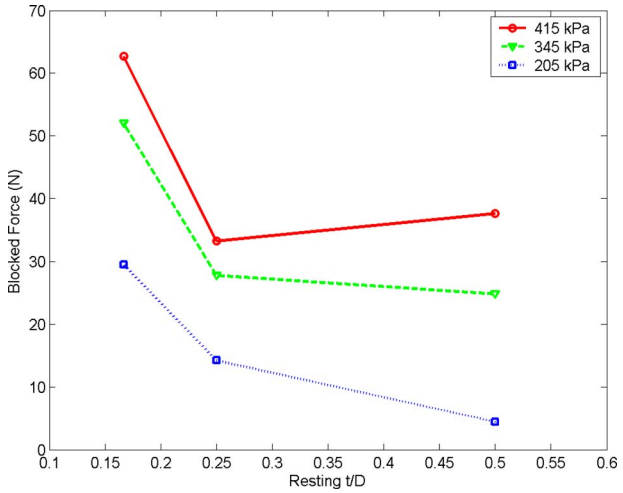

Fig. 11 Blocked force as a function of *t*/*D*—nonlinear decrease (actuator Xc)

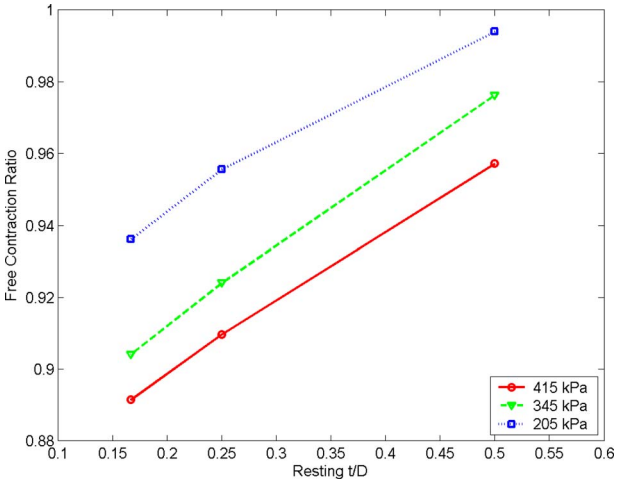

Fig. 13 Free contraction ratio as a function of *t*/*D*—linear increase (actuator Xc)

ameter increase) is larger, which could lead to interference issues in system design. Additionally, tensile stiffness also increases for PAMs with larger braid angles, and this is an important consideration for antagonistic device design.

3 Model Development

Because the activation concept of McKibben actuators is for their length to shorten under an increase in applied pressure, the longitudinal contraction ratio λ_1 is the most common means of describing this phenomenon

$$\lambda_1 = \frac{L_0 - \Delta L}{L_0} \tag{1}$$

Here, L_0 is the resting (maximum) length of the actuator, and ΔL is the change in length from the applied pressure P. Initial modeling work for these actuators considered only the kinematic relationships of the braid and assumed the system as without loss and without energy storage [3]

$$F_{\text{Gaylord}} = \frac{P}{4N^2\pi}(3(\lambda_1 L_0)^2 - B^2) = \frac{P}{4N^2\pi}(3L^2 - B^2) \tag{2}$$

where L is the length of the actuator, N is the number of turns of a single braid fiber about the actuator diameter, and B is the length of that thread. This approach was adopted more recently by researchers that extended the applicability of this model using the virtual work principle [26]. This work also used the kinematic model of Gaylord and showed that in the dynamic case, better results can be obtained when inertial effects of the fluid are considered. However, these models still suffer when comparing theoretical simulations to experimental results.

To this end, there are two modeling efforts based on different principles of physics that promise better prediction of the actuators. These include a model that accounts for elastic energy storage in the bladder [31] based on the principle of virtual work, and another model that uses Newton's second law to derive an analytical expression for the actuation force [27]. In Secs. 3.1 and 3.2, modifications to both the models will be recommended that improve their predictions considerably.

3.1 Modeling With Principle of Virtual Work. In this development, it is suggested that the force of the McKibben actuator is composed of two terms [31]. The first is the Gaylord term due

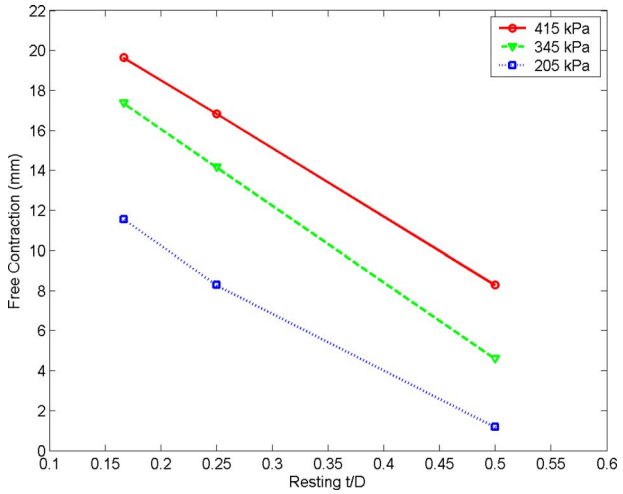

Fig. 12 Free contraction as a function of *t*/*D*—linear decrease (actuator Xc)

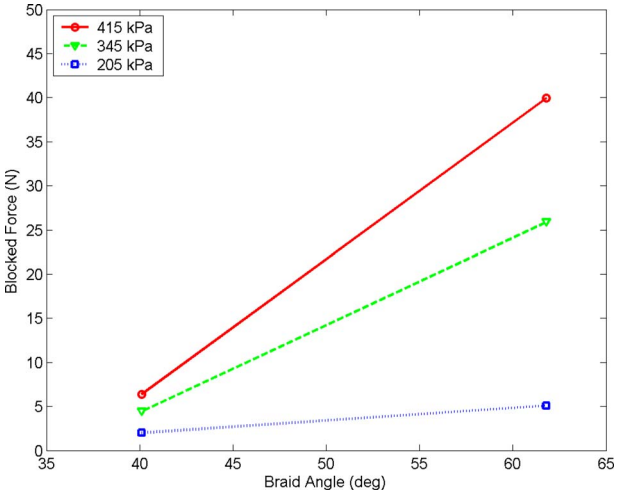

Fig. 14 Blocked force as a function of braid angle—increase (actuators 2a and 3a)

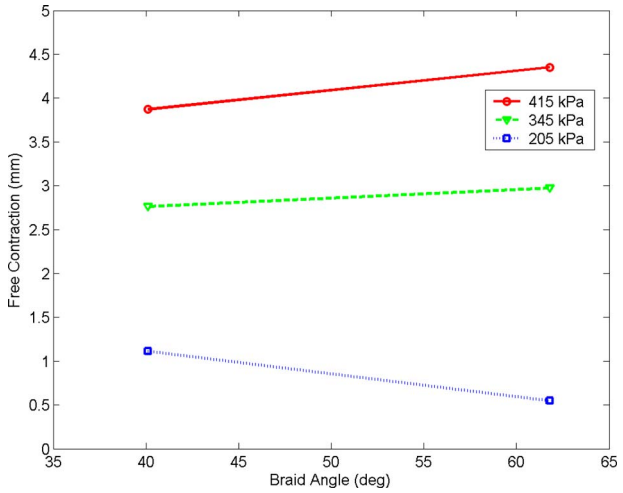

Fig. 15 Free contraction as a function of braid angle—increase (actuators 2a and 3a)

to the applied pressure and braid kinematics, and the second is a nonlinear Mooney–Rivlin term that considers the elasticity of the bladder. This equation has the form

$$F = P\frac{dV}{dL} - V_b\frac{dW}{dL} = F_{\text{Gaylord}} - F_{M-R} \tag{3}$$

where V_b is the bladder volume, and W is the strain energy density of the bladder. The expression for the Gaylord term is given in Eq. (2). To formulate the elastic energy term, a material model developed by Mooney and Rivlin [33] was incorporated. This work developed a nonlinear relationship between stress and strain that was based on geometry and material properties of rubber. This relation, which has the form

$$W = \sum_{i=0,j=0} C_{ij}(I_1 - 3)^i(I_2 - 3)^j \tag{4}$$

is a function of two strain invariants I_n and the empirical constants C_{ij} [34]. Using only two Mooney–Rivlin constants for the McKibben actuator and assuming that the bladder is incompressible yields the following expansion

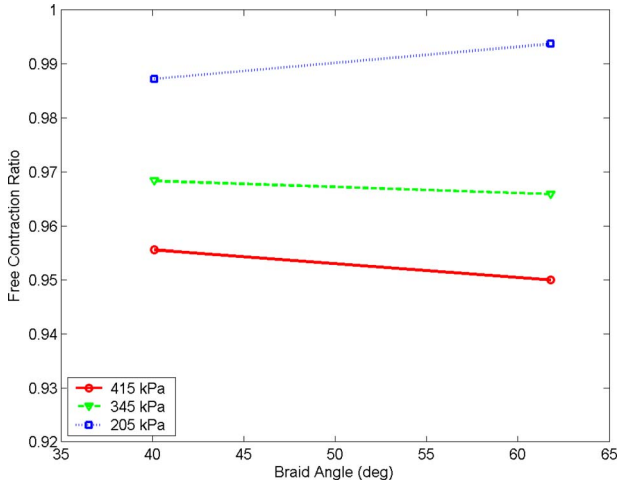

Fig. 16 Free contraction ratio as a function of braid angle—decrease (actuators 2a and 3a)

$$F_{M-R} = V_b\left\{C_{10}\left[2\lambda(1-a) - \frac{2\lambda(1+a-2a\lambda^2)}{[\lambda^2 + a\lambda^2(1-\lambda^2)]^2}\right] + C_{01}\left[2\lambda(1+a - 2a\lambda^2) - \frac{2}{\lambda^3} + \frac{2a\lambda}{[1+a(1-\lambda^2)]^2}\right]\right\} \tag{5}$$

where R_0 is the resting radius of the actuator, and the geometric parameter a is defined as

$$a = \left(\frac{L_0}{2\pi R_0 N}\right)^2 \tag{6}$$

However, simulations with this seemingly more comprehensive model show only nominal improvement in regard to matching experimental force-contraction data [31]. Though qualitatively accurate, this data showed that the nearly 90% error from using only the Gaylord term was reduced to 60% error by including the Mooney–Rivlin force term in the equation.

3.1.1 Correction of Elastic Energy Term. The expression in Eq. (5) has been derived using the constant volume assumption for the bladder. However, if we consider the definition of stretch ratios used in the previous work

$$\lambda_1 = \frac{L}{L_0}, \quad \lambda_2 = \frac{R}{R_0}, \quad \lambda_3 = \frac{1}{\lambda_1\lambda_2} \tag{7}$$

where the respective current and resting radii of the bladder tube are R and R_0, respectively; it does not consider any effects of bladder thickness. To account for these changes, the volume of the bladder at rest V_0 has the form

$$V_{b,0} = L_0[\pi R_0^2 - \pi(R_0 - t_0)^2] \tag{8}$$

where t is thickness. After inflation, the bladder volume can be expressed as

$$V_b = L[\pi R^2 - \pi(R - t)^2] \tag{9}$$

For constant volume, the resting and inflated volume must be the same, so

$$\frac{V_b}{V_{b,0}} = 1 = \lambda_1\lambda_2\lambda_3 \tag{10}$$

Modifying the second two stretch ratios from Eq. (7) to consider the average radius (mean circumference) and thickness allows the equation to better account for dimensional changes in all three directions, and has thus been shown to improve the model [35]. In the present case, defining the stretch ratios as

$$\lambda_1 = \frac{L}{L_0}, \quad \lambda_2 = \frac{R - t/2}{R_0 - t_0/2}, \quad \lambda_3 = \frac{t}{t_0} \tag{11}$$

satisfies the incompressibility condition (constant bladder volume). Derivation of the improved Mooney–Rivlin force term follows as

$$F_{cM-R} = V_b\frac{dW}{dL} = V_b\left\{2C_{10}\left[\lambda_1\frac{d\lambda_1}{dL} + \lambda_2\frac{d\lambda_2}{dL} + \lambda_3\frac{d\lambda_3}{dL}\right] + 2C_{01}\left[\lambda_1(\lambda_2^2 + \lambda_3^2)\frac{d\lambda_1}{dL} + \lambda_2(\lambda_3^2 + \lambda_1^2)\frac{d\lambda_2}{dL} + \lambda_3(\lambda_1^2 + \lambda_2^2)\frac{d\lambda_3}{dL}\right]\right\} \tag{12}$$

with the stretch ratios defined in Eq. (11), and their derivatives given by

$$\frac{d\lambda_1}{dL} = \frac{1}{L} \tag{13}$$

$$\frac{d\lambda_2}{dL} = \frac{1}{R_0 - t_0/2}\left(\frac{dR}{dL} - \frac{1}{2}\frac{dt}{dL}\right) \tag{14}$$

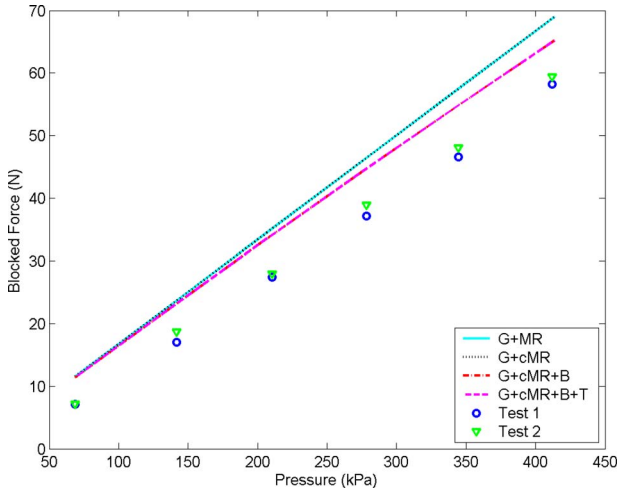

Fig. 17 Blocked force of elastic energy models compared with experimental data (actuator 5A)

$$\frac{d\lambda_3}{dL} = \frac{1}{t_0}\frac{dt}{dL} \tag{15}$$

The outer radius and thickness of the bladder can be obtained from the geometric and constant volume conditions at any time as

$$R = \frac{\sqrt{B^2 - L^2}}{2\pi N}, \quad t = R - \sqrt{R^2 - \frac{V_b}{\pi L}} \tag{16}$$

This improved expression for elastic energy improves the model significantly. It does not affect the predicted F_B (Fig. 17) because this value is defined as the force at which no contraction or reorientation has taken place ($G+MR$ and $G+cMR$ lines overlay each other), but it does influence the calculation of ΔL_F. As shown from simulations with the elastic energy term defined by Eq. (5) ($G+MR$) and Eq. (12) ($G+cMR$), Fig. 18 shows that the error in the prediction is reduced by more than 40% for an actuator of type 5a. The extent of improvement depends on the size and geometry of the actuator, with more improvement seen for smaller sizes. This size-dependent accuracy could be attributed to the fact that the significance of the elastic energy storage term depends on the volume percent of rubber.

In beginning to display model simulation results, it needs to be mentioned that the Young's modulus for the silicone rubber (2.3 MPa) and polyethylene terephthalate (PET) braid (4.3 GPa) were determined experimentally by fitting a least-squares line to the data collected for slow loading and unloading cycles of several specimens. For consistency, leftover tube material and braid were used in these tests. Bladder material was stretched to a representative amount (20%), and an apparent modulus value based on 5% maximum strain was used for the braid. For the Mooney–Rivlin parameters, published values [31] for latex rubber were used as a starting point and iterated upon using the model. The identified values are $C_{10}=1.0$ MPa and $C_{01}=-0.55$ MPa. Note that the proper identification of these parameters requires that tensile and shear specimens from the same batch of material be tested, which was not an option for the commercially available rubber used.

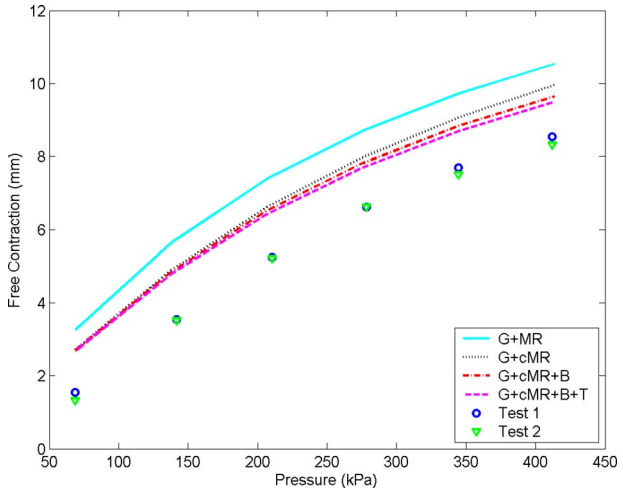

Fig. 18 Free contraction of elastic energy models compared with experimental data (actuator 5A)

3.1.2 Inclusion of Braid Effects. This concept arises because using the Gaylord equation alone or with the above correction, the blocked force prediction does not change and is much higher than experimental measurements. When the length of the actuator is kept at the resting length, the shape of the rubber tube will not change (as the braids are assumed rigid), and there are not expected to be other losses from friction or hysteresis because there is no movement involved. Hence, the possibility remains that considering elastic energy storage in the braid could improve the prediction. Other related work has also recently explored modeling braid effects, though this work focused more on the limits of contraction and friction effects [24]. In the present case, even if the length is constant, small amounts of strain may be present in the braid (and in the rubber tube) that contribute to smaller blocked force measurements.

In order to obtain an initial estimate of such elastic energy storage, only the Gaylord force term is used. The total load carried by the actuator is given by

$$F = P\frac{dV}{dL} \tag{17}$$

assuming a cylindrical shape of the actuator $V=AL$, where A is the internal cross-sectional area. Therefore,

$$F = PA + PL\frac{dA}{dL} \tag{18}$$

With the force PA taken by the air, we now assume that all the remaining force is carried by the braid (no load taken by the rubber). If the braid is composed of n fibers, the second term of Eq. (18) represents the load carried by each fiber, which becomes

$$F_{\text{braid}} = \frac{PL}{n\sin\alpha}\frac{dA}{dL} = \frac{PB}{n}\frac{dA}{dL} \tag{19}$$

through the geometry of the actuator components. The strain energy density in the braid can then be formulated as

$$W_{\text{braid}} = \frac{1}{2A_{\text{braid}}}\frac{F_{\text{braid}}}{E_{\text{braid}}}\frac{F_{\text{braid}}}{A_{\text{braid}}} = \frac{F_{\text{braid}}^2}{2E_{\text{braid}}A_{\text{braid}}^2} \tag{20}$$

where E_{braid} is the Young's modulus, and A_{braid} is the cross-sectional area of a braid fiber. Using this approach we can derive the elastic force term for the braid as

$$F_{\text{Br}} = V_{\text{Br}}\frac{dW_{\text{braid}}}{dL} = V_{\text{braid}}\frac{1}{E_{\text{braid}}A_{\text{braid}}^2 n^2}\frac{4\pi^2P^2B^2}{(2\pi N)^4}L \tag{21}$$

where the area used in the dA/dL term is $A=\pi R^2$, and the total braid volume is $V_{\text{Br}}=BnA_{\text{braid}}$. The radius was determined from the geometry of the braid with the relation

$$R^2 = \frac{(B^2 - L^2)}{(2\pi N)^2} \tag{22}$$

The actuator force is then given by

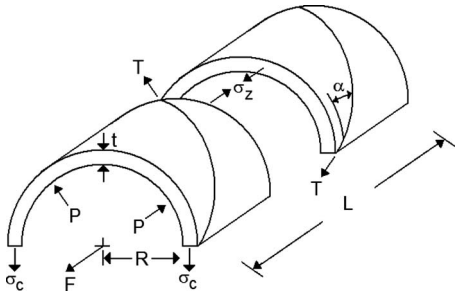

Fig. 19 Freebody diagram for force balancing model [27]

$$F = F_{\text{Gaylord}} - F_{cM-R} - F_{\text{Br}} \tag{23}$$

As apparent from the formula, braid elasticity is more significant at higher pressures and for larger actuators with longer B and L. For actuators of type 5a, the prediction error at 60 psi (415 kPa) reduces by 50% by inclusion of the F_{braid} term, which is indicated by the line denoted $G+cMR+B$ in Fig. 18.

3.1.3 Effect of Noncylindrical Tips on Energy Model. While the model assumes a cylindrical shape of the actuator throughout its pressure range, this assumption holds for the tips only at the resting condition, and the actual shape of the actuator near the tips is uncertain, though some success has been achieved using varying braid angle assumptions [32] and large deformation membrane theory [28]. In order to get an idea whether the tip shape would have an influence on the model prediction of the actuation behavior, we used a reduced length in the expression, calculating the forces in Eq. (23). It was observed during the experiments that the tips of the actuator were similar to a circular arc. Therefore, the following choice of reduced length was used

$$L' = L - \delta \tag{24}$$

$$\delta = 2(R - R_0) \tag{25}$$

Recall that R_0 is the resting radius, which remains fixed at the ends of the bladder throughout pressurization, and R is the radius of a substantially cylindrical portion (e.g., near the center) of the actuator during pressurization. The use of Eq. (24) improves ΔL_F by nearly 20% at a high pressure for actuator 5a, as denoted by the line $G+cMR+B+T$ in Fig. 18, but does not affect F_B. There is no impact on blocked force because this value assumes by definition that no contraction (tip rounding) has taken place. In summary, this term appears in the equation simply as a correction factor, though it is based on physical observation of the approximate tip shape.

3.2 Modeling With Force Balancing. In this alternative method of derivation, the force balance equation for the actuators has been derived using the freebody diagram in Fig. 19 [27]. It should be noted that a linear elastic model is formulated here, whereas the previous section employed a nonlinear elastic model to describe the actuator behavior. For force balance in the x- and z-directions, respectively,

$$PRL = \sigma_c tL + NT \cos \alpha \tag{26}$$

$$F + \pi R^2 P = \sigma_z A_{\text{rubber}} + T \sin \alpha \tag{27}$$

where here, R is the outer diameter, which does not include bladder thickness, and assumes a cylindrical shape. These equations, in conjunction with

$$\sigma = E_R \varepsilon, \quad \varepsilon_c = \frac{R}{R_0}, \quad \varepsilon_z = \frac{L}{L_0} \tag{28}$$

and geometric constraints, lead to the following expression for actuation force

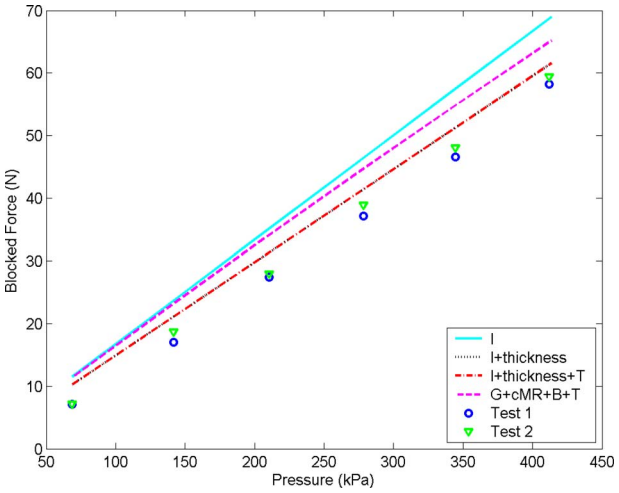

Fig. 20 Blocked force of force balance models compared with experimental data (actuator 5A)

$$F = \frac{P}{4N^2\pi}(3L^2 - B^2) - \frac{E_R t L^2}{2N^2\pi}\left(\frac{1}{R} - \frac{1}{R_0}\right) + E_R V_b\left(\frac{1}{L_0} - \frac{1}{L}\right) \tag{29}$$

where E_R is the elastic modulus for the bladder material. With Eq. (29), the prediction of F_B and ΔL_F is less accurate than with Eqs. (23) and (24), particularly for smaller actuators. Even for larger actuators like 5a, the blocked force prediction could benefit from improvement. This can be seen by lines *I* in Figs. 20 and 21. The reason for this is that the model assumes constant bladder thickness instead of constant bladder volume. It should also be noted that an experimentally determined modulus value of $E_R = 2.28$ MPa was used here.

3.2.1 Effect of Nonconstant Thickness. To include the variation in thickness in this formulation, the R terms in Eqs. (26) and (27) are modified according to

$$P(R - t)L = \sigma_c tL + NT \cos \alpha \tag{30}$$

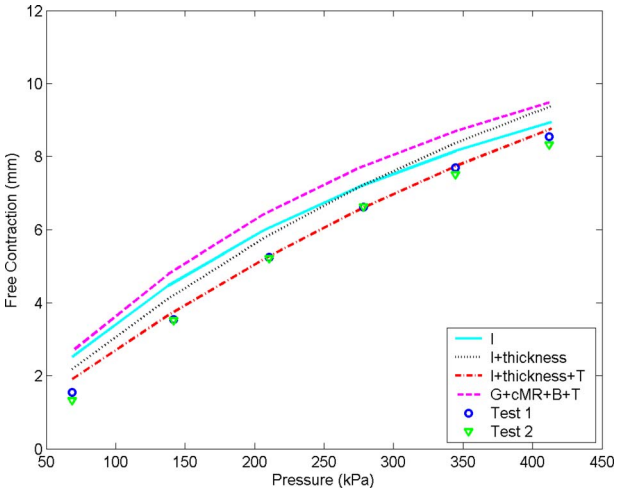

Fig. 21 Free contraction of force balance models compared with experimental data (actuator 5A)

$$F + \pi(R-t)^2 P = \sigma_z A_{\text{rubber}} + T \sin\alpha \tag{31}$$

giving the inner radius in the force balance equations. Additionally, the ε_c term in Eq. (28) is changed to consider the cross-sectional center of the bladder as

$$\varepsilon_c = \frac{R - t/2}{R_0 - t_0/2} \tag{32}$$

Note that σ and ε_z have not changed from their form in Eq. (28). Combining the modified equations (30)–(32) gives the final equation

$$F = \frac{P}{4N^2\pi}(3L^2 - B^2) + P\left(\frac{V_b}{L} - \frac{tL^2}{2\pi RN^2}\right) + E_R V_b\left(\frac{1}{L_0} - \frac{1}{L}\right) + \frac{E_R L}{2\pi RN^2}(tL - t_0 L_0) \tag{33}$$

where it should be noted that a new term has appeared in comparison to Eq. (29).

Inclusion of this thickness correction considerably improves the model prediction, surpassing the best prediction of the elastic energy models. These predictions are shown by the lines marked *I* +thickness. For smaller actuators, the error in both F_B and ΔL_F decreases significantly. In the case of larger actuators, F_B is affected much more than ΔL_F. The simulated blocked force decreases by 40% at 10 psi (70 kPa) to over 70% at 60 psi (415 kPa) for actuator 5a. Note that the *I*+thickness line is difficult to see in Fig. 20 because the *I*+thickness+*T* line overlays it. This predicted F_B is within 10% of the experimental measurements, which shows remarkable improvement in modeling the static response of McKibben actuators. However, free contraction (Fig. 21) does not change much for actuators of this size.

3.2.2 Effect of Noncylindrical Tips on Force Model. This is modeled similarly to the elastic energy case. That is, the actuator length was reduced according to Eq. (24), in conjunction with Eq. (33). With this final improvement, the error in prediction of the free contraction decreases to within 10% of the experimental data. This is evident in Fig. 21 by the lines corresponding to *I* +thickness+*T*. Similar to the energy model, inclusion of noncylindrical tip shape has no impact on the blocked force prediction here, as the *I*+thickness+*T* line completely overlaps the *I* +thickness line in Fig. 20.

3.3 Modeling Summary. It should be noted that the effect of each of the improvements mentioned above vary according to actuator size and geometry. For example, thickness or elastic energy corrections are more influential for larger t/D, and braid elasticity terms are more effective for larger α. In general, all of the above notions improve the model to different degrees for different actuators.

Based upon the preceding improvements to the energy and force balance model derivations and the data collected, it was shown that the force balance approach more accurately predicts experimental measurements. Therefore, it is suggested that the model in Eq. (33) be used with some form of accounting for tip effects, such as Eq. (24), to accurately predict the static performance of a McKibben actuator since this model provides a simple analytical expression. Additionally, the force balance model only requires knowledge of actuator dimensions and bladder stiffness, which are more readily available parameters than those of the energy balance model, such as the Mooney–Rivlin coefficients. This brings up another point, in that the two approaches here use different elastic models, which makes a direct comparison more difficult. That is, the force balance approach is linear elastic, whereas the energy balance is nonlinear elastic.

To summarize the modeling section, predictions of the improved force balance model will now be presented with experimental data from other actuator sizes to highlight its scalability over the range of parameters examined in the experimental study.

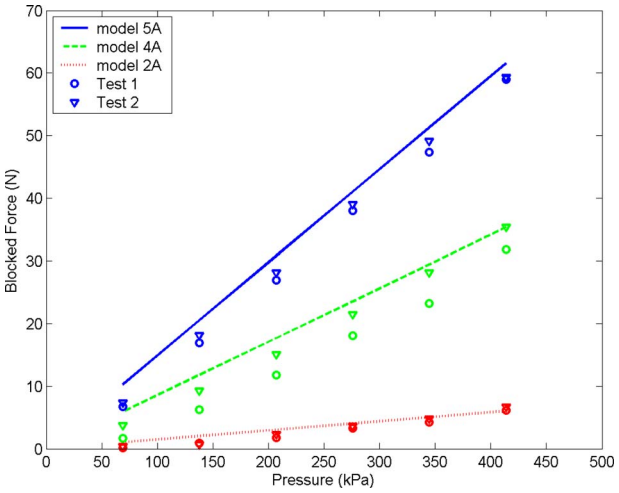

Fig. 22 Blocked force predictions using force balance model (actuator Xa)

This characterization showed that the blocked force increased with diameter. This is shown in Fig. 22, where it can be seen that the model performs well in comparison to the measured data for the three diameters tested, all at the shortest length (actuators Xa). There is a slight tendency for the model to overpredict, but the simulated values are only above the measured data by a small fraction at each of the diameters. The experimental characterization also showed that free contraction (maximum stroke) increases with actuator length. This is reflected again in Fig. 23, which shows model predictions from the largest diameter actuator at each of the three lengths tested (actuators 5x). With the accuracy exhibited in this figure and in previous in Fig. 22, validation of the improved model form is now complete.

4 Summary and Conclusions

A comprehensive set of experimental data has been presented that highlighted the static trends of McKibben actuator behavior for various geometrical changes. The general design guidelines shown state that blocked force increases with actuator diameter and is independent of length, stroke increases with length, and percent contraction is independent of length for a fixed set of actuator parameters. Regarding the initial braid angle, it was shown that actuators with larger angles can generate more force

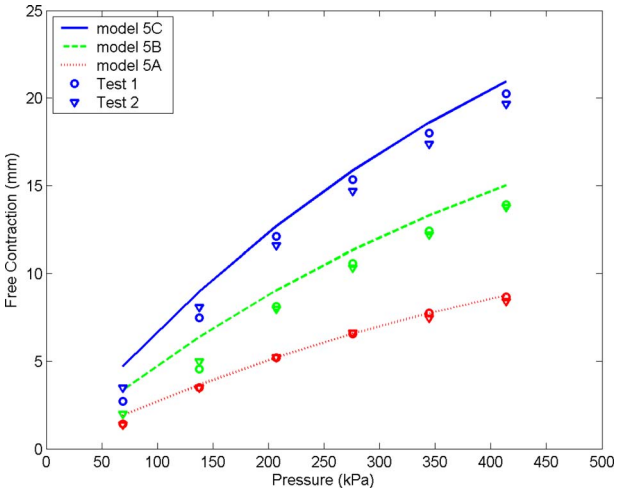

Fig. 23 Free contraction predictions using force balance model (actuator 5x)

and stroke, but this comes with a larger increase in diameter during normal operation and an increased stiffness. Another trend examined was the effect of thickness on the actuator performance metrics, which along with other experimental observations, such as noncylindrical tips, led to various improvements to existing mathematical model formulations based on energy balance and force balance derivations. Through these modifications, the improved model was validated against measured data, where it was shown to more accurately predict the static response of McKibben actuators in both free contraction and blocked force as a function of applied pressure. It was also shown that the improved force balance model performed better than the improved energy balance model. To extend the model to dynamic cases, relaxation in rubber, compressibility of the air or other working fluid, friction, and damping in the system would need to be incorporated.

Acknowledgment

This work was partially sponsored by a Phase I SBIR award from the U.S. Army Aeroflightdynamics Directorate, Contract No. W911W6-06-C-0033, with technical monitor Mark V. Fulton. The authors greatly acknowledge this support.

Nomenclature

A = cross-sectional area
α = fiber angle (radial)
B = fiber length
C_{ij} = Mooney–Rivlin coefficient
δ = length reduction factor
E = elastic modulus
ε = strain
F = force
L = actuator length
λ = contraction ratio
N = number of fiber turns
n = number of fiber threads
P = pressure
R = bladder radius
σ = stress
T = tension in fiber thread
t = bladder thickness
V = volume

References

[1] Schulte, H., 1961, "The Characteristics of the McKibben Artificial Muscles," *The Application of External Power in Prosthetics and Orthotics*, National Academy of Sciences-National Research Council, Washington, DC, pp. 94–115.
[2] Nickel, V., Perry, J., and Garrett, A., 1963, "Development of Useful Function in the Severely Paralyzed Hand," J. Bone Jt. Surg., Am. Vol., **45**(5), pp. 933–952.
[3] Gaylord, R., 1958, "Fluid Actuated Motor System and Stroking Device," U.S. Patent No. 2,844,126.
[4] Tondu, B., and Lopez, P., 1997, "The McKibben Muscle and Its Use in Actuating Robot-Arms Showing Similarities With Human Arm Behaviour," Ind. Robot, **24**(6), pp. 432–439.
[5] Klute, G., Czerniecki, J., and Hannaford, B., 2002, "Artificial Muscles: Actuators for Biorobotic Systems," Int. J. Robot. Res., **21**(4), pp. 295–309.
[6] Kerscher, T., Albiez, J., and Berns, K., 2002, "Joint Control of the Six-Legged Robot Airbug Driven by Fluidic Muscles," *Proceedings of the Third IEEE International Workshop on Robot Motion and Control*, pp. 27–32.
[7] Daerden, F., Lefeber, D., Verrelst, B., and Ham, R. V., 2001, "Pleated Pneumatic Artificial Muscles: Compliant Robotic Actuators," *Proceedings of IROS*, Vol. 4, pp. 1958–1963.
[8] Philen, M., Shan, Y., Prakash, P., Wang, K., Rahn, C., Zydney, A., and Bakis, C., 2004, "Fibrillar Network Adaptive Structure With Ion Transport Actuation," *Proceedings of ICAST*.
[9] Daerden, F., and Lefeber, D., 2002, "Pneumatic Artificial Muscles: Actuators for Robotics and Automation," European Journal of Mechanical and Environmental Engineering, **47**, pp. 10–21.
[10] Chou, C., and Hannaford, B., 1994, "Static and Dynamic Characteristics of McKibben Pneumatic Artificial Muscles," *Proceedings of ICRA*, Vol. 1, pp. 281–286.
[11] Klute, G., and Hannaford, B., 1998, "Fatigue Characteristics of McKibben Artificial Muscle Actuators," *Proceedings of IROS*, Vol. 3, pp. 1776–1782.
[12] Kingsley, D., and Quinn, R., 2002, "Fatigue Life and Frequency Response of Braided Pneumatic Actuators," *Proceedings of ICRA*, Vol. 3, pp. 2830–2835.
[13] van der Smagt, P., Groen, F., and Schulten, K., 1996, "Analysis and Control of a Rubbertuator Arm," Biol. Cybern., **75**(5), pp. 433–440.
[14] Thongchai, S., Goldfarb, M., Sarkar, N., and Kawamura, K., 2001, "A Frequency Modeling Method of Rubbertuators for Control Application in an Ima Framework," *Proceedings of the American Controls Conference*, Vol. 2, pp. 1710–1714.
[15] Schroder, J., Erol, D., Kawamura, K., and Dillman, R., 2003, "Dynamic Pneumatic Actuator Model for a Model-Based Torque Controller," *Proceedings of IEEE International Symposium on Computational Intelligence in Robotics and Automation*, Vol. 1, pp. 342–347.
[16] Tondu, B., Ippolito, S., Guiochet, J., and Daidie, A., 2005, "A Seven-Degrees-of-Freedom Robot-Arm Driven by Pneumatic Artificial Muscles for Humanoid Robots," Int. J. Robot. Res., **24**(4), pp. 257–274.
[17] Trivedi, D., Dienno, D., and Rahn, C., 2008, "Optimal, Model-Based Design of Soft Robotic Manipulator," ASME J. Mech. Des., **130**(9), p. 091402.
[18] van der Linde, R., 1999, "Design, Analysis, and Control of a Low Power Joint for Walking Robots, by Phasic Activation of McKibben Muscles," IEEE Trans. Rob. Autom., **15**(4), pp. 599–604.
[19] Colbrunn, R., Nelson, G., and Quinn, R., 2001, "Design and Control of a Robotic Leg With Braided Pneumatic Actuators," *Proceedings of IROS*, Vol. 2, pp. 992–998.
[20] Colbrunn, R., Nelson, G., and Quinn, R., 2001, "Modeling of Braided Pneumatic Actuators for Robotic Control," *Proceedings of IROS*, Vol. 4, pp. 1964–1970.
[21] Caldwell, D., and Tsagarakis, N., 2002, "Biomimetic Actuators in Prosthetic and Rehabilitation Applications," Technol. Health Care, **10**(2), pp. 107–120.
[22] Kobayashi, H., Uchimura, A., Isihida, Y., Shiiba, T., Hiramatsu, K., Konami, M., Matsushita, T., and Sato, Y., 2004, "Development of a Muscle Suit for the Upper Body—Realization of Abduction Motion," Adv. Rob., **18**(5), pp. 497–513.
[23] Sawicki, G., Gordon, K., and Ferris, D., 2005, "Powered Lower Limb Orthoses: Applications in Motor Adaptation and Rehabilitation," *Proceedings of the IEEE ICORR*, pp. 206–211.
[24] Davis, S., and Caldwell, D., 2006, "Braid Effects on Contractile Range and Friction Modeling in Pneumatic Muscle Actuators," Int. J. Robot. Res., **25**(4), pp. 359–369.
[25] Davis, S., Tsagarakis, N., Canderle, J., and Caldwell, D., 2003, "Enhanced Modelling and Performance in Braided Pneumatic Muscle Actuators," Int. J. Robot. Res., **22**(3–4), pp. 213–227.
[26] Chou, C., and Hannaford, B., 1996, "Measurements and Modeling of Mckibben Pneumatic Artificial Muscles," IEEE Trans. Rob. Autom., **12**(1), pp. 90–102.
[27] Ferraresi, C., Franco, W., and Bertetto, A., 2001, "Flexible Pneumatic Actuators: A Comparison Between the McKibben and Straight Fibres Muscles," Journal of Robotics and Mechatronics, **13**(1), pp. 56–63.
[28] Liu, W., and Rahn, C., 2003, "Fiber-Reinforced Membrane Models of McKibben Actuators," ASME J. Appl. Mech., **70**(6), pp. 853–859.
[29] Shan, Y., Philen, M., Bakis, C., Wang, K., and Rahn, C., 2006, "Nonlinear-Elastic Finite Axisymmetric Deformation of Flexible Matrix Composite Membranes Under Internal Pressure and Axial Force," Compos. Sci. Technol., **66**(15), pp. 3053–3063.
[30] Sanchez, A., Mahout, V., and Tondu, B., 1998, "Nonlinear Parametric Identification of a McKibben Artificial Pneumatic Muscle Using Flatness Property of the System," *Proceedings of the International Conference on Control Applications*, Vol. 1, pp. 70–74.
[31] Klute, G., and Hannaford, B., 2000, "Accounting for Elastic Energy Storage in McKibben Artificial Muscle Actuators," ASME J. Dyn. Syst., Meas., Control, **122**(2), pp. 386–388.
[32] Tsagarakis, N., and Caldwell, D., 2000, "Improved Modelling and Assessment of Pneumatic Muscle Actuators," *Proceedings of ICRA*, Vol. 4, pp. 3641–3646.
[33] Rivlin, R., and Saunders, D., 1951, "Large Elastic Deformations of Isotropic Materials. VII. Experiments on the Deformation of Rubber," Philos. Trans. R. Soc. London, Ser. A, **243**(865), pp. 251–288.
[34] Treloar, L., 1958, *The Physics of Rubber Elasticity*, Oxford University Press, London, England.
[35] Delson, N., Hanak, T., Loewke, K., and Miller, D., 2005, "Modeling and Implementation of McKibben Actuators for a Hopping Robot," *Proceedings of 12th International Conference on Advanced Robotics*, Vol. 12, pp. 833–840, Paper No. 70.